Gigantism in unique biogenic magnetite at the Paleocene–Eocene Thermal Maximum

Dirk Schumann[a,b], Timothy D. Raub[c], Robert E. Kopp[d], Jean-Luc Guerquin-Kern[e,f], Ting-Di Wu[e,f], Isabelle Rouiller[b,g], Aleksey V. Smirnov[h], S. Kelly Sears[b,g], Uwe Lücken[i], Sonia M. Tikoo[c], Reinhard Hesse[a], Joseph L. Kirschvink[c], and Hojatollah Vali[a,b,g,1]

[a]Department of Earth and Planetary Sciences, McGill University, 3450 University Street, Montréal, QC, Canada H3A 2A7; [b]Facility for Electron Microscopy Research, and [g]Department of Anatomy and Cell Biology, McGill University, 3640 University Street, Montréal, QC, Canada H3A 2B2; [c]Division of Geological and Planetary Sciences, California Institute of Technology, MC 170-25 1200 East California Boulevard, Pasadena, CA 91125; [d]Department of Geosciences and Woodrow Wilson School of Public and International Affairs, Princeton University, 210 Guyot Hall, Princeton, NJ 08544; [e]Imagerie Intégrative de la Molécule à l'Organisme, Institut National de la Santé et de la Recherche Médicale, Unité 759, Institut Curie, 91405 Orsay, France; [f]Laboratoire de Microscopie Ionique, Institut Curie, 91405 Orsay, France; [h]Department of Geological and Mining Engineering and Sciences, Michigan Technological University, Houghton, MI 49931-1295; and [i]Nanobiology Marketing, FEI Company, Eindhoven, 5600KA, Eindhoven, The Netherlands

Edited by James Zachos, University of California, Santa Cruz, CA, and accepted by the Editorial Board August 29, 2008 (received for review April 15, 2008)

We report the discovery of exceptionally large biogenic magnetite crystals in clay-rich sediments spanning the Paleocene–Eocene Thermal Maximum (PETM) in a borehole at Ancora, NJ. Aside from previously described abundant bacterial magnetofossils, electron microscopy reveals novel spearhead-like and spindle-like magnetite up to 4 μm long and hexaoctahedral prisms up to 1.4 μm long. Similar to magnetite produced by magnetotactic bacteria, these single-crystal particles exhibit chemical composition, lattice perfection, and oxygen isotopes consistent with an aquatic origin. Electron holography indicates single-domain magnetization despite their large crystal size. We suggest that the development of a thick suboxic zone with high iron bioavailability—a product of dramatic changes in weathering and sedimentation patterns driven by severe global warming—drove diversification of magnetite-forming organisms, likely including eukaryotes.

biomineralization | electron microscopy | magnetofossil

Magnetofossils, geologically preserved magnetic particles produced most abundantly by magnetotactic bacteria, are recognized by distinctive physical and chemical traits and provide a record of past microbial ecosystems (1–3). Two recent papers (4, 5) report an extraordinary magnetofossil "Lagerstätte" in lowermost Eocene kaolinite-rich clay sediments deposited at subtropical paleolatitude in the Atlantic Coastal Plain of New Jersey. The sediments were deposited ≈55.6 million years ago during the Paleocene–Eocene Thermal Maximum (PETM), an ≈100- to 200-ky interval of ≈5–9°C abrupt global warming (5, 6). Kopp *et al.* (4) and Lippert and Zachos (5) use ferromagnetic resonance (FMR) spectroscopy (7), other rock magnetic methods, and transmission electron microscopy (TEM) of magnetic separates to characterize sediments from boreholes at Ancora (ODP Leg 174AX) (Fig. 1) and Wilson Lake, NJ, respectively. These sediments contain abundant, ≈40- to 300-nm cuboidal, elongate-prismatic, and bullet-shaped magnetofossils, sometimes arranged in short chains, resembling crystals in living magnetotactic bacteria (4, 5). Despite scarcity of intact magnetofossil chains, the asymmetry ratios of the FMR spectra reflect a profusion of elongate SD crystals and/or chains [*FMR and Rock Magnetic Properties* in supporting information (*SI*) *Text*]. It is not obvious whether the unusual abundance of magnetofossils reflects extraordinarily favorable preservation conditions or whether ecological changes enhanced growth of magnetotactic bacteria. Here we address both conundrums by reporting the discovery from these same sediments of exceptionally large and novel biogenic magnetite crystals unlike any previously reported from living organisms or from sediments.

Results and Discussion

Scanning Electron Microscopy (SEM) and TEM. SEM and TEM analysis of the magnetic extracts reveals the presence of two large and previously unknown types of magnetofossils and uniquely large exemplars of a more common morphology. The first type of particle has a spearhead-like shape with flattened, bilateral

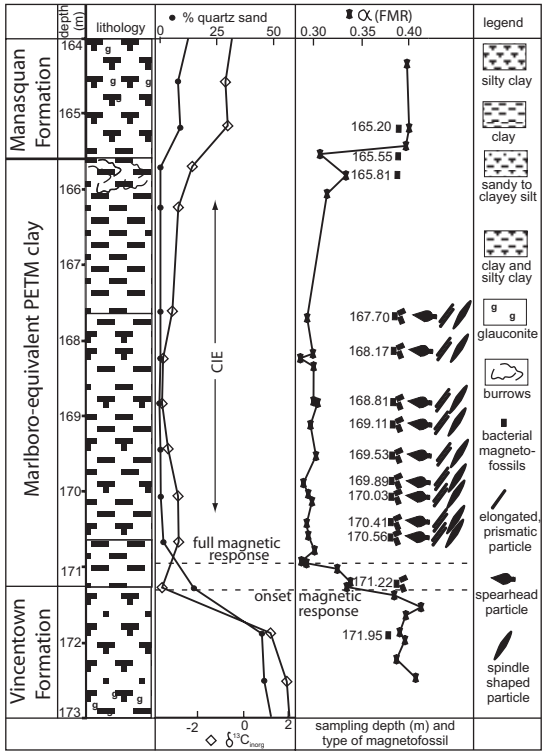

Fig. 1. Lithological profile of late Paleocene and early Eocene strata of ODP Leg 174AX, Ancora, NJ, plotted together with the fine quartz sand fraction, $\delta^{13}C_{inorganic}$, and FMR parameter α. The profile shows the abundance of different types of magnetite particles at examined sample horizons [lithological information from Miller *et al.* (37)]. Fine quartz sand fraction and $\delta^{13}C_{inorganic}$ are from Kent *et al.* (38). FMR parameter α were taken from Kopp *et al.* (4).

Author contributions: D.S. and H.V. designed research; D.S., J.-L.G.-K., T.-D.W., I.R., S.K.S., U.L., and H.V. performed research; D.S., T.D.R., R.E.K., I.R., A.V.S., S.M.T., R.H., J.L.K., and H.V. analyzed data; and D.S., T.D.R., R.E.K., S.M.T., J.L.K., and H.V. wrote the paper.

The authors declare no conflict of interest.

This article is a PNAS Direct Submission. J.Z. is a guest editor invited by the Editorial Board.

See Commentary on page 17595.

[1]To whom correspondence should be addressed. E-mail: vali@eps.mcgill.ca.

This article contains supporting information online at www.pnas.org/cgi/content/full/0803634105/DCSupplemental.

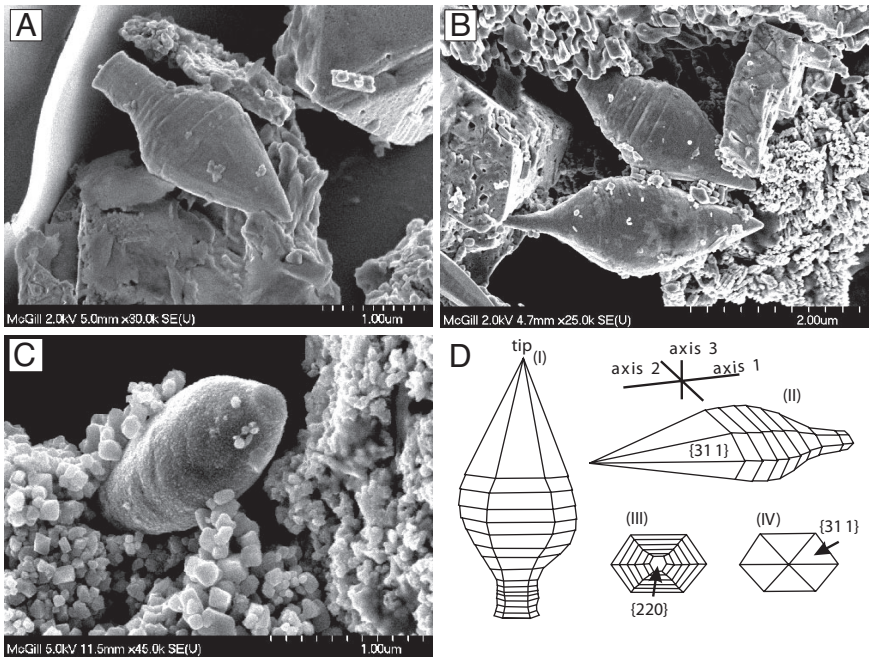

Fig. 2. SEM images and drawings showing the morphological features of the spearhead-like magnetite particles. (*A* and *B*) SEM images of spearhead-like magnetite particles with pronounced growth steps in the stalk and lower part and well developed crystal faces near the spearhead tip. (*C*) SEM image of the spearhead-like particle reveals bilateral symmetry. Note abundant conventional magnetofossils surrounding the gigantic spearhead-like particles. (*D*) Models of idealized crystal habits of the spearhead-like particle shown in *A* constructed on the basis of the lattice fringe data obtained by HRTEM. These models show the top view (I), lateral view (II), back view (III), and front view (IV).

symmetry (Fig. 2 *A–C*). These particles were possibly disaggregated from originally agglutinated, remarkable cellular armor (Fig. S1 and Movie S1). Their morphology can be described by a geometric three-axis coordinate system (Fig. 2*D*) that is not coincident with the crystallographic system. Length (axis 1) ranges from 2.0 to 3.8 μm, width (axis 2) ranges from 1.0 to 1.4 μm, and thickness (axis 3) ranges from 0.65 to 0.7 μm. The apex sector is characterized by well pronounced crystal faces resembling a six-sided pyramid-like structure.

High-resolution TEM (HRTEM) of whole particles and of an ultrathin section prepared by focused ion beam (FIB) milling reveals that the spearhead-like particles are single, defect-free crystals of magnetite (i.e., magnetofossils) (Fig. 3 and Fig. S2 *b* and *c*). The {111} lattice fringes have a *d*-spacing of 0.48 nm and are nearly parallel to the long axis (axis 1) of the particle (Fig. 3*B* and Fig. S2*c*). Another set of lattice fringes with *d*-spacing of 0.296 nm are almost parallel to less-pronounced crystal faces at the tip (Fig. 3*B*) and tail sections of the particle and correspond to {220} fringes. HRTEM images show sets of lattice fringes with *d*-spacing of 0.25 nm parallel to four pyramidal sides that correspond to the {311} family of magnetite. The middle and "stalk" sectors of some particles show circumferential steps on the crystal surfaces (Fig. 2 *A*, *B*, and *D I* and *II*) indicating ontogenetic crystal growth from "stalk" toward crystal "tip" (Fig. 4). These steps, ranging from 10 to 29 nm, are pronounced

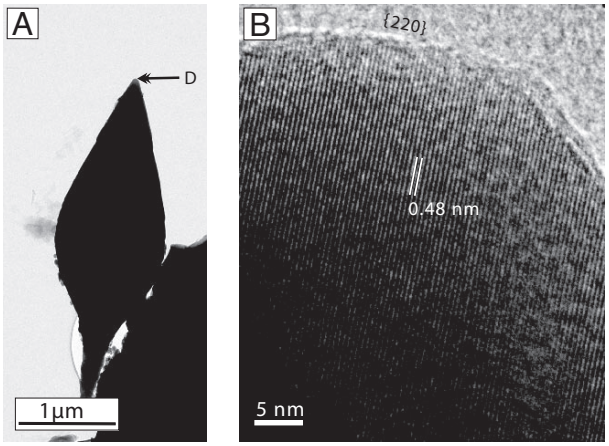

Fig. 3. Low-resolution TEM image of a random projection of a spearhead-like particle (*A*) and a HRTEM image (*B*) of the tip of the same crystal showing one set of {111} lattice fringes parallel to the long axis of the crystal. High-resolution images of the tip area also reveal the presence of {220} crystal faces.

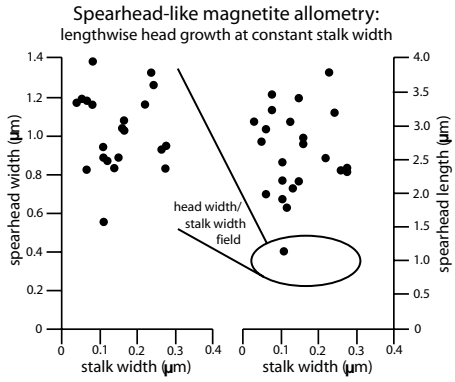

Fig. 4. Allometry of the spearhead-like particles. Variance in stalk width and spearhead width are both ≈3.6% of those respective means. Variance in spearhead length, by contrast, is >15% of mean spearhead length, suggesting that spearhead-like particles continue to grow lengthwise after they reach a (perhaps itinerantly) maximum width and maintain a constant proportion between stalk and spearhead. This allometry is consistent with the sense of elongation required by assumed epitactic growth forming the tipward-convex, surface ''step'' features on both stalk and spearheads.

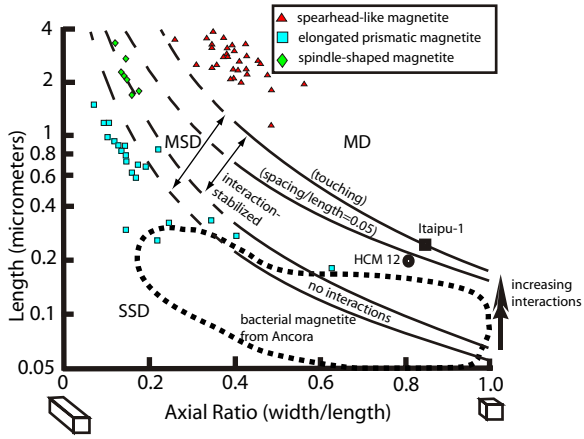

Fig. 5. Domain-stability diagram of the upper limit for SD magnetization calculated from micromagnetic models of prismatic magnetite crystals (39). Interaction effects and chain arrangements increase this upper size limit, and shape anisotropy stabilizes SD behavior for any given maximum crystal size. The largest magnetosome crystals yet observed from living bacteria are indicated: the largest cuboidal particles from strain Itaipu-1 (40) and the largest hexaoctahedral prisms and bullet particles from the Ammersee and Moorsee, respectively (9). The large, unusual PETM magnetofossils of elongate hexaoctahedral and spindle-like morphologies are mostly stable single domain (SSD) or metastable single domain (MSD). We hypothesize that unusual crystal-tip truncations of these forms impede development of the metastable flower-like structure magnetization. Spearhead-like magnetite crystals are of a size that should be multidomain, attesting to the likelihood of their nonmagnetotactic biological function. Other considerations suggest that these crystal forms may have been used for protection by iron-biomineralizing eukaryotes.

in some particles. Numerous crystal fragments show parting along a {220} plane (Fig. S3), consistent with rare observations of large, untwined magnetite crystals under stress (8). Energy dispersive x-ray spectroscopy shows chemical composition consistent with magnetite (Fig. S4).

Whereas the dimensions of the spearhead-like particles are outside the SSD range for magnetite parallelepipeds (Fig. 5), electron holographic analysis reveals a uniform, centrally symmetric magnetization with electromagnetic field lines emerging at the tip of the particle (Fig. 6). Although the appearance of SD structure might reflect a metastable state imparted during the magnetic concentration process, we hypothesize that the crystal morphology could stabilize the SD state by inhibiting the development of "flower structures."

The second novel crystal morphology observed in these samples is spindle-like and tapered at each end (Fig. 7). This type of particle has a width of 0.5 μm and a length of up to 3.3 μm.

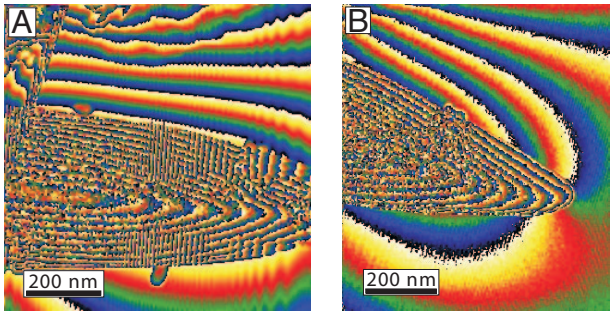

Fig. 6. Contour images obtained from the magnetic contribution to the holographic phase for the spearhead-like magnetite particles. (*A*) Center-symmetric, uniform-magnetized particle. (*B*) Electromagnetic field lines emerging from the tip of the same particle.

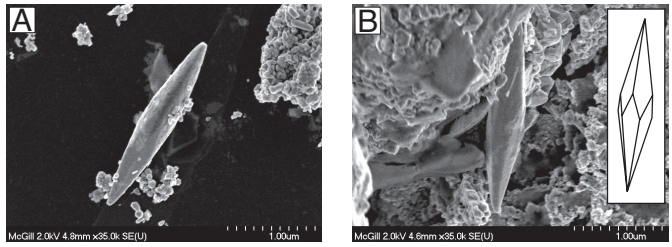

Fig. 7. SEM images show tapered, spindle-like magnetite particles with well developed crystal faces. The crystal morphology suggests a six-sided trapezohedron habit (*Inset* in *B*).

Both ends of the particle exhibit well pronounced crystal faces resembling a six-sided trapezohedron. The third crystal habit is an extremely long, defect-free hexaoctahedral crystal with well developed crystal faces and a length-to-width ratio as high as ≈10 (Figs. 5 and 8). Lattice-fringe images and energy dispersive x-ray spectroscopy analyses (Fig. S4) of both the second and third types of particle also suggest chemical composition and structure consistent with magnetite. Their size and shape imply that these crystals lie within the SD (SSD) stability field of magnetite (Fig. 5). Crystal type three appears to be similar to elongate hexaoctahedral magnetosome crystals described from living bacteria and magnetofossils but stretched up to ≈1.4 μm in length. By contrast, the largest such crystals described from bacteria of Quaternary Bahamian sediments are ≈170 nm long (9), and the longest magnetofossil reported previously is ≈580 nm in length (M. W. Hounslow, personal communication). Unlike most bacterial magnetite, however, these particles have been observed not in chains, but rather in isolation or in aggregates of originally isolated crystals (Fig. 8*A* and Fig. S2*a*).

Oxygen Isotopes. To constrain the crystallization temperature of the spearhead-like particles, we measured the oxygen isotopic composition of individual crystals using NanoSIMS (Fig. 9). The primary goal of this analysis was to assess whether the particles could have been formed at the low temperatures necessary for a biogenic origin. Assuming that the magnetic particles were formed at low temperature in equilibrium with calcite produced by benthic foraminifera, we used the calcite–water fractionation equation of O'Neil *et al.* (10) and the bacterial magnetite–water fractionation of Mandernack *et al.* (11) to derive a calcite–magnetite fractionation equation and estimate a paleotemperature of magnetite formation (Table S1). Benthic foraminifera of the taxa *Cibicidoides* from the PETM interval at Wilson Lake, NJ, have a $\delta^{18}O_{VPDB}$ of approximately −3.0‰ (12). By coupling

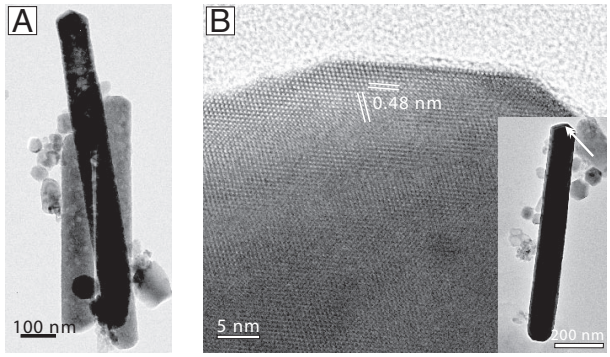

Fig. 8. TEM images show an overview (*A*) and lattice fringes (*B*) of elongated hexaoctahedral magnetite particles. The lattice-fringe image (*B*) of the tip of an individual crystal (*Inset*) shows two sets of defect-free {111} lattice fringes with *d*-spacings of 0.48 nm.

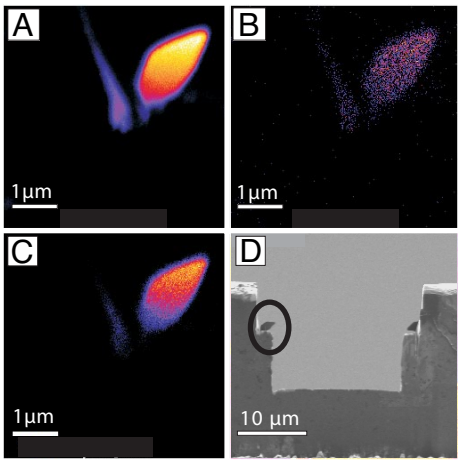

Fig. 9. Images of a spearhead-like particle prepared by focused ion beam milling. False-color NanoSIMS images of the $^{16}O^-$ (*A*), $^{18}O^-$ (*B*), and FeO^- (*C*) composition of one of the spearhead-like magnetite particles milled in half by the FIB. Bright colors (white or yellow) indicate higher amounts of the measured oxygen isotopes or iron oxide. The SEM image (*D*) shows the copper grid with two spearhead-like particles mounted with tungsten to the grid. The analyses were performed on the particle outlined by the circle.

carbonate and magnetite isotopic measurements (Table S1) we calculated a 1-standard deviation (σ) temperature range of −5° to 34°C. Owing to the imprecision of current measurement techniques, we are unable to improve upon prior benthic temperature estimates, but our calculated 1σ temperature range (−5° to 34°C) is consistent with previous estimates from carbonate oxygen isotopes and from the TEX-86 organic biomarker proxy (24–34°C) (12). Our mean $\delta^{18}O_{VSMOW}$ estimate of −1.2‰ is distinct from that of metamorphic magnetite (approximately +15‰) in regional highlands at Franklin Furnace and Sterling Hill, NJ (13).

Speculation on Origin and Function. Owing to the cubic crystal symmetry of magnetite, abiogenic magnetite formed at high temperature most commonly exhibits octahedral morphology. Unusual asymmetric habits and whiskers have been reported from exsolution processes, crystallization in anisotropic environments such as lava flows (14), and high-temperature, vapor-phase crystallization (15). Low-temperature anisotropic morphologies, however, are known only from biologically controlled systems (16). Magnetite biomineralization was originally discovered in chiton teeth (17), where magnetite provides a hard mineral for scraping limestone. It has subsequently been found in magnetotactic bacteria (18), algae (19), honey bees, homing pigeons, fish, and even the human brain (20). In all these latter cases, the morphology, size, structural arrangement, and even the magnetic sensory function resemble closely those of particles produced by magnetotactic bacteria that may show isometric cubooctahedral and elongate hexaoctahedral habits, as well as irregular and elongate bullet, tooth, and arrowhead-like shapes.

Because the spearhead- and spindle-like particles exhibit a complex, nonequidimensional, anisotropic morphology and low-temperature isotopic composition, an abiogenic origin is unlikely. Allometric inferences bolster the case for biogenicity (Fig. 4). Variation of both stalk width and spearhead width of spearhead-like particles spans only ≈3.6% of the mean values for those measures. Spearhead-length variance, by contrast, exceeds 15% of mean spearhead length. Uniform three-dimensional growth, even at different rates along long and short axes, could not produce this asymmetric size variance. This pattern would be produced, however, if the spearhead-like particles continued to grow lengthwise after reaching a (possibly itinerant) maximum width, with constant proportion of stalk and spearhead widths. Such allometric growth is also consistent with the sense of elongation required by assumed epitactic growth forming the tipward-convex, surface "step" features on both stalk and spearheads (Fig. 2 *A* and *B*).

Because the size of these crystals is the same as or exceeds the size of most bacteria, they are likely the products of eukaryotes. The single-crystal particles identified here have dimensions in the realm of skeletal elements, such as silica in diatoms and radiolaria, carbonate or silica in sponge spicules, or iron phosphates in holothurian spicules (21), although they are chemically and morphologically dissimilar in detail from any modern or other fossil analogues (*Paleontology Searching for Modern Analogues* in *SI Text*). We are unaware of any other biogenic structure of these sizes and shapes. The biological function of these new magnetite particles is uncertain; the organisms that formed them could have used the particles for their magnetic properties or, as in chiton teeth (17), for their hardness. A few apparently intact, tip-outward assemblages of the spearhead-like particles (Fig. S1 and Movie S1), and the inference of shear-induced parting of individual spearhead crystals (Fig. S3), suggest that these forms may have served a structural purpose, perhaps as protective armor surrounding an ≈5- to 10-μm cell.

Environmental Implications. The abundance of fossil magnetotactic bacteria on the Atlantic Coastal Plain during the PETM (4, 5) could be explained by enhanced production, enhanced preservation, or both. The presence of novel, large, presumably eukaryotic magnetofossils argues that changes in growth conditions are a major part of the explanation. Considering that bacterial magnetofossils are also present (although less abundant) and well preserved in the sediments below and above the PETM clay (Fig. S5) as well as in a sand lens within PETM clay (4), the presence of these new forms in the PETM clay is unlikely to be a preservation artifact. There is also no evidence for extensive dissolution of magnetofossils, similar to that observed in some marine sediments, within or outside of the PETM (3). No modern or other fossil analogs of the organisms that formed the giant magnetofossils have yet been found (*Paleontology Searching for Modern Analogues* in *SI Text*).

Together with the bacterial magnetofossils, the presence of these new magnetite forms suggests that global warming at the PETM drove locally dramatic changes in the biogeochemical cycling of iron, resulting in an enlarged, meter-scale suboxic zone (22, 23). Just as the ready availability of iron sulfide at hydrothermal vents has permitted the evolution of animals using magnetic iron sulfides to construct protective structures (24), the high availability of iron in a thick suboxic zone may have fostered the growth, and perhaps evolutionary radiation, of magnetotactic and other iron-biomineralizing organisms.

Several lines of evidence suggest a global trend toward enhanced surface productivity during the PETM. *Apectodinium*, a dinoflagellate taxa that has a heterotrophic motile stage believed to be associated with higher productivity, spreads globally from a low-latitude source during the PETM (25). Bathyal sediments from several sites in the Tethys, Atlantic, and Southern Oceans show an increase in biogenic barium, a tracer of organic matter export from surface to deep water (26, 27). [On the other hand, nanofossils from bathyal sediments in the central Pacific indicate a transition from a late-Paleocene oligotrophic environment to a highly stressed, presumably severely nutrient-limited environment during the PETM (28).]

At Wilson Lake, consistent with enhanced nutrient delivery to the coastal plain, oligotrophic nanofossil taxa are replaced with mesotrophic taxa for the entire duration of the PETM (28). Notably, the *Apectodinium* acme occurs during the onset of the carbon isotopic excursion, the first ≈15% of the ≈16-m interval

recording the carbon isotope excursion (29). A short-lived spike in organic carbon content (to ≈0.8 wt%) occurs near the end of this interval, followed by a dip to near-zero organic carbon comparable in duration to the *Apectodinium* acme, which is in turn followed by a return to the relatively low late Paleocene organic carbon levels of ≈0.4 wt% (5).

Although magnetotactic bacteria can thrive in the meter-scales oxic–anoxic transition zones of eutrophic water columns (e.g., refs. 30 and 31), such environments are not ideal for the preservation of magnetofossils. The organic-rich sediments deposited under such conditions promote reductive dissolution (1, 31). In contrast, suboxic but organic-lean sediments provide ideal conditions for both the growth and preservation of magnetofossils.

Possible analog environments, combining high surface productivity with low-organic carbon density sediments and meter-scale sedimentary suboxic zones (32), are provided by tropical shelves fed by energetic river systems, such as the Amazon (33). Because of intense tropical weathering, the supply of reactive iron in such settings is approximately double that of temperate deltaic environments (34). Physical reworking, which facilitates the reoxidation of iron and thereby enhances its effective supply as an oxidant, also plays an important role in establishing a thick suboxic zone. During the PETM, similar dynamics may have developed in an Appalachian-fed deltaic system along the Atlantic Coastal Plain of New Jersey, although the energy level of the delta need not have been as great as that of tropical systems, given evidence for a low supply of terrestrial organic carbon (12) and thus reduced oxidant demand. In addition to the sedimentary and nanofossil evidence for enhanced runoff discharge to the New Jersey continental shelf (12, 29), this analog is also consistent with the intense weathering conditions that promote kaolinite development (35). Abrupt establishment of such an environment indicates the power of a ≈5–9°C global warming event to reshape sedimentary and biological processes.

Methods

Transmission Electron Microscopy (TEM) Analysis. Magnetic separates were extracted (2) from 15 samples of the Ancora drillcore (ODP Leg 174AX) ranging from 165.20 m to 173.15 m in depth (Fig. 1). The separates were transferred onto 300-mesh Cu TEM grids with carbon support film and studied by using either the JEOL JEM-2000FX TEM at 80 kV or the JEOL-JEM 2100F FE-TEM at 200 kV, the latter equipped with an Oxford INCA microanalytical system, and a Hitachi S-4700 FE-STEM at accelerating voltages ranging from 2 to 5 kV and an emission current of 15 μA.

FIB Milling. Three spearhead-like magnetite particles were separated from the magnetic extract by using a microsampling device in a Hitachi FB-2000A FIB system and mounted on a half-circular copper grid for ion milling. One particle was ion-milled to a thickness of ≈100 nm for lattice-fringe imaging and selected-area electron diffraction. Two other particles were milled from one side to create a smooth surface for oxygen isotopic analyses.

Elemental Mapping (O, Fe) and Oxygen Isotope (^{18}O, ^{16}O) Analysis by Nanosecondary Ion Mass Spectrometry (NanoSIMS). Oxygen isotopic ratios were measured by using a NanoSIMS-50 microprobe (Cameca) at an operating current of ≈1 pA. Ion images for $^{16}O^-$ and $^{18}O^-$, as well as for FeO^- (for monitoring Fe distribution), were generated by using an image definition of 128 × 128 pixels while a Cs^+ beam was scanned over a field of view of 5 μm × 5 μm. The images acquired through NanoSIMS analysis for $^{16}O^-$ and for $^{18}O^-$ were used to calculate the isotopic ratio of $^{18}O/^{16}O$ pixel-to-pixel. To provide precise measurement of the isotopic ratio of $^{18}O/^{16}O$ on the magnetite crystal, a long acquisition time was used. This was achieved by acquiring 95 frames with a dwell time of 3 ms per pixel for each frame. The total counting time per pixel was 60–75 ms. The acquired image series was then processed by using ImageJ, a public domain Java Image processing program. For each frame, a new image representing the ratio of ^{18}O to ^{16}O for each pixel was generated by dividing the image of $^{18}O^-$ to the one of $^{16}O^-$. During this operation, all of the $^{16}O^-$ images were corrected with the dead-time loss (44 ns) of the detection system owing to the high ion intensity for this major isotope. SIMS analysis generally requires the use of a reference standard for quantitative measurement. In this analysis, we used the surface oxide on the copper mounting grid as a reference. Owing to the limited number of measurements, there is a wide range of isotopic variation. The relative error for a single measurement is 0.58% (or 5.8‰). To achieve a precision of 1‰, 30 measurements for a total time of 8–9 h would be required.

Off-Axis Electron Holography. Off-axis electron holography was performed in a FEI Tecnai G^2 F20 X-Twin TEM at an accelerating voltage of 200 kV. The electron holograms were obtained at a biprism voltage of 105 V by using the Lorentz lens and recorded with a Gatan Ultrascan 1000 CCD camera at the nominal microscope magnification of ×1,500. The contour images of the magnetic contribution to the holographic phase were obtained according to the procedure of Midgley (36).

ACKNOWLEDGMENTS. We gratefully acknowledge comments from Boswell Wing, Adam Maloof, Nicholas Swanson-Hysell, and Harunur Rashid and technical assistance from Jeannie Mui. We are grateful to the editor and three anonymous reviewers for their constructive comments, which improved the final version of the manuscript. This work was supported by grants from the Natural Science and Engineering Research Council of Canada and the Fonds Québécois de la Recherche sur la Nature et les Technologies to the Centre for Biorecognition and Biosensors (H.V.) and the NASA Exobiology program (J.L.K.). Samples were provided by the Ocean Drilling Program, which is sponsored by the U.S. National Science Foundation and by participating countries under management of Joint Oceanographic Institutions, Inc.

1. Kopp RE, Kirschvink JL (2008) The identification and biogeochemical interpretation of fossil magnetotactic bacteria. *Earth Sci Rev* 86:42–61.
2. Petersen N, von Dobeneck T, Vali H (1986) Fossil bacterial magnetite in deep-sea sediments from the South-Atlantic Ocean. *Nature* 320:611–615.
3. Vali H, Kirschvink JL (1989) Magnetofossil dissolution in a paleomagnetically unstable deep-sea sediment. *Nature* 339:203–206.
4. Kopp RE, *et al.* (2007) Magnetofossil spike during the Paleocene–Eocene thermal maximum: Ferromagnetic resonance, rock magnetic, and electron microscopy evidence from Ancora, New Jersey, United States. *Paleoceanography*, doi: 10.1029/2007PA001473.
5. Lippert PC, Zachos JC (2007) A biogenic origin for anomalous fine-grained magnetic material at the Paleocene–Eocene boundary at Wilson Lake, New Jersey. *Paleoceanography*, doi: 10.1029/2007PA001471.
6. Bowen GJ, *et al.* (2006) Eocene hyperthermal event offers insight into greenhouse warming. *Trans Am Geophys Union* 87:165–169.
7. Kopp RE, *et al.* (2006) Chains, clumps, and strings: Magnetofossil taphonomy with ferromagnetic resonance spectroscopy. *Earth Planet Sci Lett* 247:10–25.
8. Greig JW, Merwin HE, Posnjak E (1936) Separation planes in magnetite. *Am Mineral* 21:504–510.
9. Vali H, Kirschvink JL (1990) in *Iron Biominerals*, eds Frankel RB, Blakemore RP (Plenum, New York), pp 97–115.
10. O'Neil JR, Clayton RN, Mayeda TK (1969) Oxygen isotope fractionation in divalent metal carbonates. *J Chem Phys* 51:5547–5558.
11. Mandernack KW, Bazylinski DA, Shanks WC, Bullen TD (1999) Oxygen and iron isotope studies of magnetite produced by magnetotactic bacteria. *Science* 285:1892–1896.
12. Zachos JC, *et al.* (2006) Extreme warming of mid-latitude coastal ocean during the Paleocene–Eocene Thermal Maximum: Inferences from TEX86 and isotope data. *Geology* 34:737–740.
13. Johnson CA, Skinner BJ (2003) Geochemistry of the furnace magnetite bed, Franklin, New Jersey, and the relationship between stratiform iron oxide ores and stratiform zinc oxide-silicate ores in the new Jersey Highlands. *Econ Geol Bull Soc* 98:837–854.
14. Ma C, Rossman GR, Miller JA (2007) The origin of color in ''fire'' obsidian. *Can Mineral* 45:551–557.
15. Bradley JP, Harvey RP, McSween HY (1996) Magnetite whiskers and platelets in the ALH84001 Martian meteorite: Evidence of vapor phase growth. *Geochim Cosmochim Acta* 60:5149–5155.
16. Mann S, Sparks NHC, Blakemore RP (1987) Structure, morphology and crystal-growth of anisotropic magnetite crystals in magnetotactic bacteria. *Proc R Soc London B* 231:477–487.
17. Lowenstam HA (1962) Magnetite in denticle capping in recent chitons (Polyplacophora). *Geol Soc Am Bull* 73:435–438.
18. Blakemore R (1975) Magnetotactic Bacteria. *Science* 190:377–379.
19. de Araujo FFT, Pires MA, Frankel RB, Bicudo CEM (1986) Magnetite and magnetotaxis in algae. *Biophys J* 50:375–378.
20. Kirschvink JL, Hagadorn JW (2000) in *The Biomineralisation of Nano- and Micro-Structures*, ed Bäuerlein E (Wiley-VCH, Weinheim, Germany), pp 139–150.
21. Lowenstam HA (1989) Spicular morphology and mineralogy in some Pyuridae (Ascidiacea). *Bull Mar Sci* 45:243–252.
22. Dickens GR, Francis JM (2004) Comment on ''A case for a comet impact trigger for the Paleocene/Eocene thermal maximum and carbon isotope excursion.'' *Earth Planet Sci Lett* 217:197–200.
23. Dickens GR (2008) Palaeoclimate: The riddle of the clays. *Nat Geosci* 1:86–88.

24. Suzuki Y, *et al.* (2006) Sclerite formation in the hydrothermal-vent ''scaly-foot'' gastropod—possible control of iron sulfide biomineralization by the animal. *Earth Planet Sci Lett* 242:39–50.
25. Crouch EM, *et al.* (2001) Global dinoflagellate event associated with the late Paleocene thermal maximum. *Geology* 29:315–318.
26. Schmitz B, Charisi SD, Thompson EI, Speijer RP (1997) Barium, SiO2 (excess), and P2O5 as proxies of biological productivity in the Middle East during the Palaeocene and the latest Palaeocene benthic extinction event. *Terra Nova* 9:95–99.
27. Bains S, Norris RD, Corfield RM, Faul KL (2000) Termination of global warmth at the Palaeocene/Eocene boundary through productivity feedback. *Nature* 407:171–174.
28. Gibbs SJ, *et al.* (2006) Shelf and open-ocean calcareous phytoplankton assemblages across the Paleocene–Eocene Thermal Maximum: Implications for global productivity gradients. *Geology* 34:233–236.
29. Sluijs A, *et al.* (2007) Environmental precursors to rapid light carbon injection at the Palaeocene/Eocene boundary. *Nature* 450:1218–1221.
30. Simmons SL, *et al.* (2004) Spatiotemporal distribution of marine magnetotactic bacteria in a seasonally stratified coastal salt pond. *Appl Environ Microbiol* 70:6230–6239.
31. Kim BY, Kodama KP, Moeller RE (2005) Bacterial magnetite produced in water column dominates lake sediment mineral magnetism: Lake Ely, USA. *Geophys J Int* 163:26–37.
32. Aller RC, Blair NE (2006) Carbon remineralization in the Amazon-Guianas tropical mobile mudbelt: A sedimentary incinerator. *Cont Shelf Res* 26:2241–2259.
33. Aller RC (1998) Mobile deltaic and continental shelf muds as suboxic, fluidized bed reactors. *Mar Chem* 61:143–155.
34. Aller RC, Hannides A, Heilbrun C, Panzeca C (2004) Coupling of early diagenetic processes and sedimentary dynamics in tropical shelf environments: The Gulf of Papua deltaic complex. *Cont Shelf Res* 24:2455–2486.
35. Gibson TG, Bybell LM, Mason DB (2000) Stratigraphic and climatic implications of clay mineral changes around the Paleocene/Eocene boundary of the northeastern US margin. *Sediment Geol* 134:65–92.
36. Midgley PA (2001) An introduction to off-axis electron holography. *Micron* 32:167–184.
37. Miller KG, *et al.* (1999) *Proceedings of the Ocean Drilling Program*, eds Miller KG, *et al.* (Ocean Drilling Program, College Station, TX), pp 1–65.
38. Kent DV, *et al.* (2003) A case for a comet impact trigger for the Paleocene/Eocene thermal maximum and carbon isotope excursion. *Earth Planet Sci Lett* 211:13–26.
39. Muxworthy AR, Williams W (2006) Critical single-domain/multidomain grain sizes in noninteracting and interacting elongated magnetite particles: Implications for magnetosomes. *J Geophys Res Solid Earth*, 111:B12S12, doi: 10.1029/2006JB004588.
40. Spring S, *et al.* (1998) Phylogenetic affiliation and ultrastructure of uncultured magnetic bacteria with unusually large magnetosomes. *Arch Microbiol* 169:136–147.